Impact of dimensionless numbers on the efficiency of magnetorotational instability induced turbulent transport

G. Lesur, Pierre-Yves Longaretti

Impact of dimensionless numbers on the efficiency of magnetorotational instability induced turbulent transport

G. Lesur[★] and P.-Y. Longaretti

Laboratoire d'Astrophysique, Observatoire de Grenoble, BP 53, 38041 Grenoble Cedex 9, France

ABSTRACT

The magnetorotational instability (MRI) is presently the most promising source of turbulent transport in accretion discs. However, some important issues still need to be addressed to quantify the role of MRI in discs; in particular no systematic investigation of the role of the physical dimensionless parameters of the problem on the dimensionless transport has been undertaken yet. For completeness, we first generalize existing results on the marginal stability limit in the presence of both viscous and resistive dissipation, exhibit simple scalings for all relevant limits, and give them a physical interpretation. We then re-examine the question of transport efficiency through numerical simulations in the simplest setting of a local, unstratified shearing box, with the help of a pseudo-spectral incompressible 3D code; viscosity and resistivity are explicitly accounted for. We focus on the effect of the dimensionless magnetic field strength, the Reynolds number and the magnetic Prandtl number. First, we complete existing investigations on the field strength dependence by showing that the transport in high magnetic pressure discs close to marginal stability is highly time dependent and surprisingly efficient. Secondly, we bring to light a significant dependence of the global transport on the magnetic Prandtl number, with $\alpha \propto Pm^{\delta}$ for the explored range: $0.12 < Pm < 8$ and $200 < Re < 6400$ (δ being in the range 0.25–0.5). We show that the dimensionless transport is not correlated to the dimensionless linear growth rate, contrary to a largely held expectation. For large enough Reynolds numbers, one would expect that the reported Prandtl number scaling of the transport should saturate, but such a saturation is out of reach of the present generation of supercomputers. Understanding this saturation process is nevertheless quite critical to accretion disc transport theory, as the magnetic Prandtl number Pm is expected to vary by many orders of magnitude between the various classes of discs, from $Pm \ll 1$ in young stellar object discs to $Pm \gtrsim$ or $\gg 1$ in active galactic nucleus discs. More generally, these results stress the need to control dissipation processes in astrophysical simulations.

Key words: accretion, accretion discs – MHD – turbulence.

1 INTRODUCTION

Angular momentum transport has always been a central issue in accretion disc theory. The first α model (Shakura & Sunyaev 1973) already assumed the presence of strong turbulent motions, modelled through an effective viscosity, orders of magnitude larger than the expected disc molecular viscosity. Since then, the physical origin of this turbulence has been highly debated. As purely hydrodynamic non-stratified Keplerian flows are known to be linearly stable to small perturbations, a finite-amplitude instability was first envisioned to trigger turbulence. This question was studied both experimentally (Richard & Zahn 1999; Richard 2001) and numerically (Balbus, Hawley & Stone 1996; Hawley, Balbus & Winters 1999),

leading to a long controversy. More recent numerical and experimental investigations of this problem strongly support the idea that the transport due to this mechanism, if present, would be far too inefficient to account for the short disc evolution time-scales imposed by astrophysical observations (Lesur & Longaretti 2005; Ji et al. 2006). Linear instabilities of hydrodynamic origin have also been envisioned as a source of turbulence, relating in particular to the flow stratification (Klahr & Bodenheimer 2003; Urpin 2003; Dubrulle et al. 2005; Shalybkov & Ruediger 2005), but these are either not present or too inefficient (Arlt & Urpin 2004; Johnson & Gammie 2006; Longaretti & Lesur, in preparation; see Lesur & Longaretti 2005 and references therein for a recent review of this issue).

The potential role of magnetohydrodynamic (MHD) instabilities in accretion discs was pointed out in a seminal paper by Balbus & Hawley (1991), devoted to an analysis of what is now known as

★E-mail: geoffroy.lesur@obs.ujf-grenoble.fr

the magnetorotational instability (MRI). This instability has been extensively studied since then, mainly with the help of local (Hawley, Gammie & Balbus 1995; Stone et al. 1996) and global (Hawley 2000) 3D numerical simulations. Although a more recent set of numerical simulations did focus on MRI energetics (Gardiner & Stone 2005), the dissipation of turbulent fields in these simulations is not controlled, as no physical term was introduced to account for physical viscosity and resistivity. Note however that Brandenburg et al. (1995) have introduced such dissipation in their simulations, but kept it as small as possible, and in any case did not try to investigate their effect in a systematic way. Resistivity effects alone have also been introduced by Fleming, Stone & Hawley (2000), but viscous effects were still neglected. This raises questions about the exact role of numerical dissipation in all these simulations, especially in the light of our recent investigation of subcritical turbulence in accretion discs (Lesur & Longaretti 2005), which clearly showed that a careful control of dissipation and resolution – and more generally of the dimensionless parameters of the problem – is required to properly quantify turbulent transport.

This issue is addressed here in the context of MRI-driven turbulence, using a 3D spectral Fourier code, which allows a precise monitoring of viscous, resistive and numerical dissipation. First, we recall the MHD equations in the shearing sheet framework (Hawley et al. 1995), along with the relevant dimensionless parameters of the problem, and summarize what is known about their effect on MRI-induced turbulent transport. Next, we investigate the linear stability of the MRI, which to the best of our knowledge has not been fully characterized when both viscosity and resistivity are accounted for in the dispersion relation. Then, we present new results on the behaviour of turbulent transport in the dimensionless parameters regime that has not been investigated in the past: first, very close to the threshold of instability (in terms of relative magnetic field strength), and then with respect to the magnetic Prandtl number, which has been ignored in all previous investigations. The dependence of turbulence transport on the magnetic Prandtl number is the most significant finding of this investigation. This dependence may turn out to be critical, as the magnetic Prandtl number varies by many orders of magnitude in astrophysical discs. The astrophysical implications of our findings are further discussed in our concluding section, along with potential caveats relating to numerical limitations that may influence our results.

2 SHEARING BOX CHARACTERIZATION AND SUMMARY OF EARLIER RESULTS

The MRI has already been extensively studied in the literature (see e.g. Balbus 2003, and references therein for a review of the subject). Our objective is to extend previous work through a systematic exploration of the dependence of the MRI-induced transport on the physical quantities characterizing the problem. For simplicity, we work in a shearing sheet setting (see Hawley et al. 1995 for a description of the shearing box equations, numerical boundary conditions and conserved quantities); vertical stratification is ignored, but both viscous and resistive microphysical (molecular) dissipation are included. This differs from previous investigations, where this is always ignored. Our previous experience with subcritical hydrodynamic transport has shown us that the inclusion of explicit dissipation is required to precisely characterize transport properties and to sort out converged simulations from under-resolved ones (see Lesur & Longaretti 2005 for an extensive discussion and illustration of these points).

The problem is formulated in a Cartesian frame centred at $r = R_0$, rotating with the disc at $\Omega = \Omega(R_0)$ with radial dimension $H \ll R_0$. In this work, H is the size of our simulation boxes, in the vertical and radial dimensions. This leads to the following set of equations, assuming $\phi \to x, r \to -y$:

$$\partial_t \boldsymbol{u} + \boldsymbol{u} \cdot \nabla \boldsymbol{u} = -\frac{1}{\rho}\nabla P + \frac{1}{\mu_0 \rho}(\nabla \times \boldsymbol{B}) \times \boldsymbol{B},$$
$$- 2\boldsymbol{\Omega} \times \boldsymbol{u} - 2\Omega S y \boldsymbol{e_y} + \nu \Delta \boldsymbol{u}, \tag{1}$$

$$\partial_t \boldsymbol{B} = \nabla \times (\boldsymbol{u} \times \boldsymbol{B}) + \eta \Delta \boldsymbol{B}, \tag{2}$$

$$\nabla \cdot \boldsymbol{u} = 0, \tag{3}$$

$$\nabla \cdot \boldsymbol{B} = 0, \tag{4}$$

where the medium is defined by $S = -r\partial_r\Omega$. For simplicity, incompressible motions are assumed. This is a priori justified by the fact that MRI-induced motions are usually subsonic, so that one expects at least in first approximation that compressibility effects do not play a major role in the problem. This approximation allows us to remove the flow Mach number from the list of dimensionless parameters characterizing the problem, so that we can more effectively isolate and quantify the role of the various physical agents.

The terms on the right-hand side of equation (1) are the gas pressure, Lorentz force, Coriolis force, tidal force and viscous dissipation, respectively. The steady-state solution to this equation is the local profile $\boldsymbol{u} = Sy\,\boldsymbol{e_x}$ with $S = 3/2\Omega$ for Keplerian discs. In the remainder of this paper, we will use the deviation from the laminar profile $\boldsymbol{w}$ defined by $\boldsymbol{w} = \boldsymbol{u} - Sy\boldsymbol{e_x}$. For simplicity, we assume that the steady-state magnetic field B_0 lies along the vertical axis. Note that this field is also the average field in the shearing sheet box, and is conserved during the evolution thanks to the shearing sheet boundary conditions (Hawley et al. 1995).

These equations are characterized by four dimensionless numbers; the first three are related to the Navier–Stokes equation while the last one belongs to the induction equation.

(i) The Reynolds number, $Re \equiv SH^2/\nu$, measures the relative importance of non-linear coupling through the advection term and viscous dissipation.

(ii) A proxy to the plasma β parameter, defined here as $\beta = S^2 H^2/V_A^2$ where $V_A^2 = B_0^2/\mu_0\,\rho$ is the Alfvén speed. The rationale of this definition follows from the vertical hydrostatic equilibrium constraint $c_s \sim \Omega H$, which is expected to hold in thin discs, so that our definition of β is indeed related to the plasma parameter in an equivalent, vertically stratified disc. This parameter measures the relative weight of the Lorentz force and the advection term.

(iii) The rotation number (inverse Rossby number), defined as $R_\Omega = 2\Omega/S$, which measures the relative importance of the Coriolis force.

(iv) The magnetic Reynolds number, $Rm = SH^2/\eta$, which measures the relative importance of resistive dissipation with respect to the ideal term in the induction equation.

We consider only Keplerian discs in this investigation, so that the rotation number is held fixed to its Keplerian value $R_\Omega = -4/3$. This leaves us with three independent dimensionless numbers: β, Re and Rm.

On the other hand, the (local in the disc) dimensionless transport coefficient,

$$\alpha = \frac{\langle v_x v_y - B_x B_y/(\mu_0\rho)\rangle}{S^2 H^2}, \tag{5}$$

being a dimensionless number, can only depend on the local dimensionless parameters characterizing the flow that we have just defined[1] (the bracketing refers to appropriate box and/or time averages). Our task reduces to characterizing this dimensionless transport as a function of the three independent dimensionless numbers just defined. However, for later convenience, we take them to be β, Re and $Pm \equiv \nu/\eta = Rm/Re$ instead (the rationale of this latter choice will become apparent later on).

All previous investigations ignore the dependence on the last two dimensionless numbers, which have not been included in the physical description up to now. Within such an approximation, Hawley et al. (1995) have characterized the dependence of α on β. Their results imply that

$$\alpha \simeq 3\beta^{-1/2}, \tag{6}$$

from their equations (10), (15), (16) and (18).

This implies in particular that α increases when the initial (and box-average) magnetic field B_0 is increased. However, for a large enough field, the smallest unstable wavelength (which increases along with B_0) becomes larger than the box size, and the instability is quenched. On this basis, one expects that the scaling equation (6) would break down close enough to the critical β stability limit. This question is somewhat investigated in the present work. However, most of our effort is devoted to characterizing the Re and Pm dependence of α.

3 LINEAR STABILITY ANALYSIS

In order to quantify the MRI-induced turbulent transport, it is first necessary to define the parameter domain in which this instability operates. The linear stability of differentially rotating discs in the presence of a magnetic field was first investigated in the astrophysical context by Balbus & Hawley (1991). Then, the instability in the weakly ionized case was considered (Blaes & Balbus 1994; Wardle 1999; Balbus & Terquem 2001), leading to the well-known dead zone problem (Gammie 1996). However, we are not aware of any reasonably complete and heuristically clarified investigation of the stability limits of the fluid when both viscous and resistive dissipation are taken into account. Some discussions of this point are available in the literature, mostly motivated by liquid-metal experiments, in the limit $Pm \ll 1$ (Ji, Goodman & Kageyama 2001; Rüdiger & Shalybkov 2002). However, these papers exhibit no clear asymptotical limit that may be useful for astrophysical discs. Therefore, we provide such an analysis here, as a prelude to our non-linear simulations.

We will consider only axisymmetric perturbations, so that we can eliminate the azimuthal perturbation transport term. Note that this assumption does not seem to have a great influence on the stability limit, since 3D numerical simulations and linear analysis of axisymmetric modes exhibit nearly the same stability limit; this holds in particular in the simulations presented here.

We linearize and Fourier transform the equations of motion by assuming $\boldsymbol{v} = \boldsymbol{v_0} \exp[i(\omega t - k_y y - k_z z)]$ and $\boldsymbol{b} = \boldsymbol{b}_0 \exp[i(\omega t - k_y y - k_z z)]$. This yields the following linearized equation set:

$$(i\omega + \nu k^2)\boldsymbol{v_0} = i\boldsymbol{k}\psi - i\,k_z \frac{B_0}{\mu_0 \rho_0}\boldsymbol{b_0}$$
$$+ (2\Omega - S)v_y \boldsymbol{e_x} - 2\Omega v_x \boldsymbol{e_y}, \tag{7}$$

---

[1] It may also depend on the simulation aspect ratio and resolution, from a numerical point of view.

$$(i\omega + \eta k^2)\boldsymbol{b_0} = -i\,k_z B_0 \boldsymbol{v} + b_y S\boldsymbol{e_x}, \tag{8}$$

$$i\boldsymbol{k} \cdot \boldsymbol{v} = 0, \tag{9}$$

$$i\boldsymbol{k} \cdot \boldsymbol{B} = 0, \tag{10}$$

where ψ is the perturbation in total pressure $(P + B^2/\mu_0)/\rho$. Introducing $\omega_\nu \equiv \omega - i\,\nu\,k^2$ and $\omega_\eta \equiv \omega - i\,\eta\,k^2$, the Alfvén speed $V_A^2 = B_0^2/\mu_0\rho$, the epicyclic frequency $\kappa^2 = 2\Omega(2\Omega - S)$ and $\gamma^2 = k_z^2/k^2$, one eventually gets the dispersion relation:

$$\left(\omega_\nu\omega_\eta - k_z^2 V_A^2\right)\left[\omega_\nu^2\omega_\eta^2 - 2\omega_\nu\omega_\eta k_z^2 V_A^2 - \omega_\eta^2\kappa^2\gamma^2\right.$$
$$\left. - k_z^2 V_A^2\left(2\Omega S\gamma^2 - k_z^2 V_A^2\right)\right] = 0 \tag{11}$$

which we now solve in various dissipation regimes.

3.1 $Pm = 1$ behaviour

Let us first look at the $Pm = 1$ case, where the dispersion equation can be solved exactly by analytical means. The condition $\Im(\omega) < 0$ expresses the existence of the instability, and implies that the MRI exists if and only if $\nu^2 k^4 < -\omega_\nu^2$. From this constraint and the dispersion relation (11), one finds that

$$\nu^2 < \frac{\sqrt{\kappa^4\gamma^4 + 16k_z^2 V_A^2 \Omega^2\gamma^2}}{2k^4} - \frac{k_z^2 V_A^2}{k^4} - \frac{\kappa^2\gamma^2}{2k^4} \tag{12}$$

is a necessary and sufficient criterion for instability. One can check that the highest ν values are obtained when $\gamma = 1$ and $k_z = \min(k_z) = 2\pi/H$, which corresponds to the so-called channel flow solution in the z-direction. From our definition of the Reynolds number as $Re = SH^2/\nu$ where H is the numerical box height or the typical disc height, and of the plasma parameter $\beta = S^2H^2/V_A^2$, the stability limit equation (12) translates into a relation between these two parameters, represented in Fig. 1.

Note that the instability has two different limits, depending on the β parameter.

(i) A high-β regime, corresponding to a low magnetic pressure. In this regime, marginal stability occurs at a characteristic Reynolds number value $Re_c \simeq 80$. This behaviour illustrates that the growth time-scale of the most unstable mode must be shorter than the dissipation time-scale, defined by $\tau_d \simeq k^2/\nu$.

(ii) A low-β regime, which is nearly Reynolds independent. In this region, one can define a critical $\beta(\beta_c = 29.5)$ for which the MRI is lost. This behaviour can be explained by considering the unstable mode of shortest wavelength: as β goes to smaller values, the smallest unstable wavelength increases (see equation 12). At some point it becomes larger than the scaleheight H (or box size in our
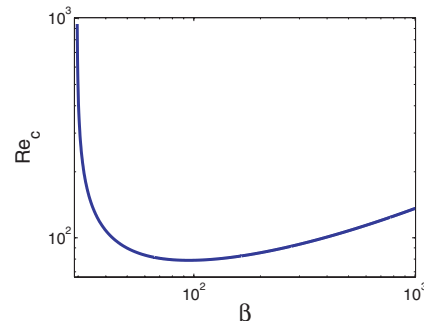

Figure 1. MRI linear stability limit for $Pm = 1$.

case) and the instability is lost. Since this phenomenon takes place at large scales, the Reynolds number plays little or no role. Note that this regime is not specific to our unstratified calculation, since similar results are found for a stratified medium where marginal stability usually occurs for $\beta_c \gtrsim 1$ (see e.g. Balbus & Hawley 1991; Gammie & Balbus 1994). This limit is reached when the last factor in equation (11) cancels out, that is, when $2\Omega S = V_A^2 k_z^2$ (the usual dissipationless MRI-stability limit).

3.2 $Pm \neq 1$ behaviour

The dispersion relation can no longer be solved exactly in this case, but an approximate solution can be found in the low magnetic field limit ($V_A \to 0$, or more precisely $V_A k_z \ll \kappa$), where marginal stability follows from a balance between the destabilizing term, and the dissipation ones. The 'opposite' (high-β) marginal stability limit, where destabilization is balanced by the usual Alfvénic magnetic tension, is briefly addressed at the end of this section.

In the limit of vanishing magnetic field, the dispersion relation has two relevant roots $\omega_\eta^2 = 0$ and $\omega_\nu^2 = \kappa^2$. In what follows, we refer to these roots as the Alfvénic and the inertial branch, respectively. Looking for the first-order correction in $V_A^2 k_z^2$ to the Alfvénic branch yields the following result, which describes the MRI modes:

$$\omega = i\eta k_z^2 \pm i \left[\frac{2\Omega S}{k_z^4 (\eta - \nu)^2 + \kappa^2} \right]^{1/2} V_A k_z. \tag{13}$$

Note that viscosity and resistivity do not play a symmetric role in this expression. Two interesting limits with respect to the magnitude of the viscosity prove useful to characterize marginal stability. As before, we maximize instability by assuming $\gamma = 1$ and $k_z = 2\pi/H$.

3.2.1 Low-viscosity limit

First consider the limit where $\nu k_z^2 \ll \kappa$. In this case, equation (13) reduces to $\eta k^2 = (2\Omega\, S/\kappa^2)^{1/2} V_A k_z$ (where $\eta k_z^2 \ll \kappa$ has been self-consistently used). Using the Lundquist number defined as $Lu = Rm\beta^{-1/2}$, this can be recast as

$$Lu = \left(\frac{2\pi}{3^{1/2}} \right) \simeq 3.6. \tag{14}$$

Note that our definition of the Lundquist number is not strictly identical to Turner, Sano & Dziourkevitch (2007) but is widely used in the MHD community.[2] In this regime, the $\omega_\eta^2\kappa^2$ term balances the $2\Omega SV_A^2 k_z^2$ term in the dispersion relation (11). Equation (14) corresponds to the limit found by Fleming et al. (2000). It is also related to the origin of the 'dead zone' in accretion discs (see e.g. Gammie 1996). This marginal stability limit is relevant to discs with low Prandtl numbers ($Pm \ll 1$) and high Reynolds numbers ($Re \gg 1$), such as young stellar object (YSO) discs.

Also, for negligible resistivity, growth rates in this regime are given by

$$\tau^{-1} \simeq \frac{1}{2\pi} \left(\frac{2\Omega S}{\kappa^2} \right) V_A k_z. \tag{15}$$

This result is valid for $V_A k_z \lesssim \kappa$ due to our expansion scheme; it also gives the correct order of magnitude of maximum growth

---

[2] The difference lies in the fact that our calculation is made in the limit of high β, leading to a linear growth rate controlled by V_A instead of Ω.

---

rates when $V_A k_z \sim \kappa$, as shown by the standard dissipationless MRI analysis.

3.2.2 High-viscosity limit

Conversely, consider the large viscosity limit, where $\nu k^2 \gg \kappa$. The corresponding relations in this limit are

$$Re\,Rm = \frac{3^{1/2}}{2} (2\pi)^3 \beta^{1/2} \simeq 215\beta^{1/2} \tag{16}$$

and

$$\tau^{-1} \simeq \frac{1}{2\pi} \left(\frac{2\Omega S}{\nu k_z^2} \right) V_A k_z. \tag{17}$$

In this regime, the $\omega_\nu^2\omega_\eta^2$ term balances the $2\Omega SV_A^2 k_z^2$ term in the dispersion relation (11). The growth rates relevant here are much smaller than those in the small-viscosity limit, equation (15). In fact, equation (13) indicates that this is the case as soon as $\nu k_z^2 \lesssim \kappa$, or equivalently, for the largest mode, when

$$Re \gtrsim \frac{3(2\pi)^2}{2} \simeq 60. \tag{18}$$

This limit divides the low- and high-viscosity regimes.

The marginal stability limit equation (16) obtains for large Prandtl and small Reynolds numbers. In the large Prandtl ($Pm \gg 1$) and large Reynolds number limit ($Re \gg 1$) expected in active galactic nucleus (AGN) discs, the growth rates of equation (15), or more generally of dissipationless MRI, are recovered. As before, these growth rates are expected to be valid (in order of magnitude) for $V_A k_z \lesssim \kappa$ due to our expansion scheme.

Note finally that a similar analysis can be performed for the inertial modes, but is not very informative; as they appear to be always stable.

3.2.3 High-β limit

Although we did not investigate this case in much detail, it is apparent from equation (11) that when $2\Omega S = V_A^2 k_z^2$ (cancellation of the last term in equation 11), $\omega_\eta = 0$ is one of the solutions to the dispersion relation. In the light of our preceding analyses, and because this equality embodies the MRI-stability limit in the ideal case, as recalled above, it is apparent that this relation is the relevant limit in a small dissipation context as well, generalizing the result found for $Pm = 1$.

3.2.4 Heuristic explanation

To explain the behaviour brought to light in equations (14) and (16), it is useful to recall the physical origin of the instability, as discussed, for example, in Balbus & Hawley (2003), in the dissipation-free limit; the process is sketched in Fig. 2, for convenience. Assume for definiteness that one starts by distorting the equilibrium velocity field in the radial direction with a sinusoidal perturbation in the vertical direction: $v_y = v_{y_0} \exp(-ikz)$. The magnetic field being frozen in the fluid will also develop a radial component [first term in the right-hand side of the linearized induction equation, i.e. equation (8)]; the shear will then transform this radial field into an azimuthal one [second term in the right-hand side of the linearized induction equation, i.e. equation (8)]. The resulting tension force produces a momentum transfer between fluid
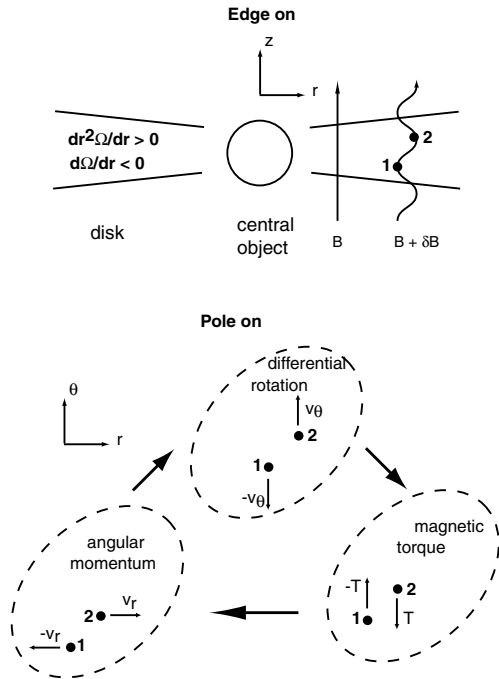
Figure 2. Sketch of the MRI mechanism (see text).

particles that have been moved according to the imposed velocity perturbation [second term in the right-hand side of the linearized motion equation, i.e. equation (8)]. This force is destabilizing if the angular velocity decreases with radius: indeed in this case, the inner particle, moving faster than the outer one, will transfer orbital momentum to the outer one, thereby reinforcing its inward motion, an effect mediated by the Coriolis force when seen in the rotating frame. In this description, marginal stability follows when the driving mechanism is balanced by the usual tension restoring force (the piece not connected to the generation of magnetic field from the mean shear).

What does dissipation change in this picture? For definiteness, let us focus on marginal stability and let us consider only resistive dissipation for the time being ('low'-viscosity limit). In this limit, the magnitude of the velocity and magnetic fields in the various steps of the instability mechanism described above are controlled by dissipation processes so that one may again go through the preceding process step by step, assuming equilibrium at each step. The magnitude of the radial magnetic field in this context results from the balance between the motion driving and field dissipation:

$$-ikB_0 v_y = \eta k^2 b_y, \tag{19}$$

while the shearing generation of the azimuthal field from the radial one is also balanced by resistive dissipation:

$$Sb_y = \eta k^2 b_x. \tag{20}$$

Both relations follow from the induction equation in the marginal stability limit, except for the term dropped in equation (20), which leads to the usual magnetic tension stabilization and is of no interest in the limit considered here. The azimuthal force balance then requires that

$$(2\Omega - S)v_y = i\frac{kB_0}{\mu_0\rho_0}b_x, \tag{21}$$

that is, $\omega_\eta^2\kappa^2 = 2\Omega SV_A^2 k^2$, once the two preceding constraints are taken into account (inclusion of ω in this line of argument does not

change the result). As noted earlier, this relation directly leads to equation (14).

If one assumes instead that viscous dissipation exceeds the Coriolis force in magnitude, then the magnetic tension due to the generation of azimuthal field from the radial one by the shear should be balanced by viscous dissipation instead of the Coriolis force in the two horizontal components of the momentum equation, leading alternatively to $\omega_\eta^2\omega_\nu^2 = 2\Omega SV_A^2 k^2$, that is, to equation (16).

This also relates to the structure of MRI modes. In the limit of a very small magnetic tension restoring force, the Alfvénic branch is made of b_x dominated modes. The other components of the magnetic field and the velocity field are of the order of $V_A k$ compared to b_x. Therefore, the growth rate is at first controlled by the dissipation rate of b_x, which is related to the resistivity (first term of the right hand side of equation 13). The interaction of the other fields, which leads to the MRI, is controlled by a term symmetric in ν and η (second term of equation 13).

3.2.5 Generic behaviour

A more complete view of the stability limits and growth rates implied by equation (11) may be obtained from exact numerical solutions for $Pm \neq 1$. Expressing this dispersion relation in terms of ω leads to the condition

$$\begin{aligned}
\omega^4 &- 2ik^2\omega^3(\eta + \nu) - \omega^2[a + k^4(\eta^2 + \nu^2 + 4\eta\nu) + b] \\
&+ \omega[2ik^6(\eta\nu^2 + \nu\eta^2) + aik^2(\nu + \eta) + 2ib\eta k^2] \\
&+ \nu^2\eta^2k^8 + a\nu\eta k^4 + b\eta^2k^4 - c = 0,
\end{aligned} \tag{22}$$

with

$$a = 2k_z^2 V_A^2, \tag{23}$$

$$b = \kappa^2\gamma^2, \tag{24}$$

$$c = k_z^2 V_A^2 (2\Omega\gamma^2 S - k_z^2 V_A^2). \tag{25}$$

To characterize the stability limits as a function of the Reynolds (Re) and the magnetic Reynolds numbers ($Rm = SH^2/\eta$), one needs to choose β, γ and k_z. As in the $Pm = 1$ case, we take $k_z = 2\pi/H$ and $\gamma = 1$ (which are again expected to maximize the dissipation limits), and solve the relation (22) for $\beta = 10^4$. The resulting stability limits are shown in Fig. 3 and the corresponding growth rates in Fig. 4 (arbitrary units). These results match closely the analytical limits just discussed: a high Re threshold found for $Rm \sim 371$, and a low
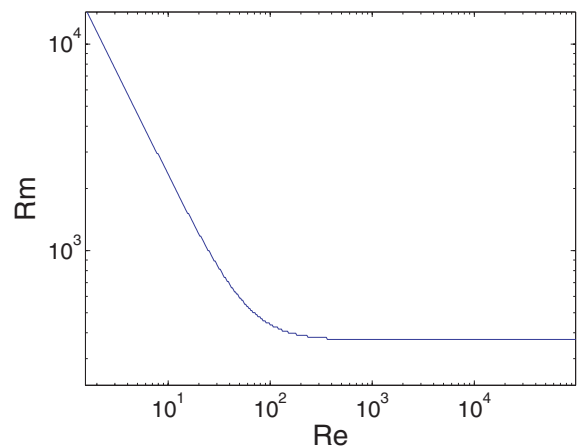

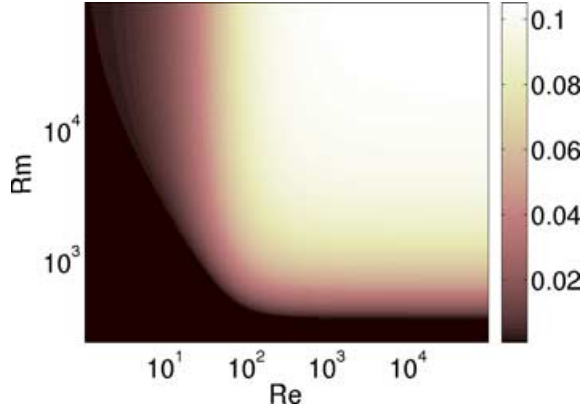**Figure 3.** MRI linear stability limit in the $Pm \neq 1$ case for $\beta = 10^4$.

Figure 4. MRI growth rate (arbitrary unit) as a function of viscous and resistive dissipation for $\beta = 10^4$.

Re threshold found for *Rm Re* $\sim 2.3 \times 10^4$, both in agreement with equations (14) and (16), respectively. Moreover, significantly lowered growth rates are observed when $Re \ll 60$–80, as predicted by equations (17) and (18). A similar behaviour follows at much smaller β. For example, the observed scalings are identical, and the preceding asymptotic expressions valid within a factor of 2, down to β values of the order of twice the critical β limit.

These results indicate that most of the stability limit behaviour is captured by the approximate relations (14) and (16) (as well as by the large-field β limit, where relevant), whose physical origin has been discussed above.

3.3 Numerics

3.3.1 Equations

Our objective is to simulate the system of equations (1) and (2), with the incompressibility condition (3), to characterize the dependence of turbulent transport on the main dimensionless numbers introduced above (β, *Re* and *Pm*). We focus on incompressible motions; indeed, the values of α found in previous investigations make us a priori expect that compressibility effects will be small. In any case, this allows us to more effectively distinguish the effects of the various physical mechanisms at work in this problem.

First, we simplify the problem from a numerical point of view by distinguishing the mean laminar shear $\boldsymbol{u} = Sy\boldsymbol{e}_x$ from the deviation from this mean $\boldsymbol{w}$. The resulting equations read

$$\partial_t \boldsymbol{w} + \boldsymbol{w} \cdot \nabla \boldsymbol{w} = -Sy\partial_x \boldsymbol{w} - \nabla \psi + \frac{\boldsymbol{B} \times (\nabla \times \boldsymbol{B})}{\mu_0 \rho_0}$$
$$+ (2\Omega - S)w_y \boldsymbol{e}_x - 2\Omega w_x \boldsymbol{e}_y + \nu \Delta \boldsymbol{w},$$
$$\partial_t \boldsymbol{B} + \boldsymbol{w} \cdot \nabla \boldsymbol{B} = -Sy\partial_x \boldsymbol{B} + \boldsymbol{B} \cdot \nabla \boldsymbol{w} + B_y S \boldsymbol{e}_x + \eta \Delta \boldsymbol{B},$$
$$\nabla \cdot \boldsymbol{w} = 0,$$
$$\nabla \cdot \boldsymbol{B} = 0.$$

This system is numerically solved using a full 3D spectral code, using the classical shearing sheet boundary conditions (Hawley et al. 1995). This code is now briefly described.

3.3.2 Numerical code

The code used for these simulations is an MHD extension of the HD code used in Lesur & Longaretti (2005), and extensively described

there. This code is a full 3D spectral (Fourier) code, based on FFTW libraries, parallelized using the MPI protocol. This kind of code has many advantages for the simulation of incompressible turbulence, such as:

(i) The incompressibility and solenoid conditions are easily implemented at machine precision, using a projector function in Fourier space.

(ii) The energy budget is much easier to control, leading to a precise quantification of the energy losses by numerical dissipation.

(iii) Spatial derivatives are very accurate down to the grid scale (equivalent to an infinite order finite difference scheme down to the grid scale).

The algorithm used is a classical pseudo-spectral method which may be described as follows. All the derivatives are computed in Fourier space. However, the non-linear term requires special treatment: in Fourier space, a real-space product is a convolution, for which the computational time evolves as n^2, where *n* is the number of grid cells. The computation time is minimized if one goes back to real space, computes the needed product and then transforms the result to Fourier space. This procedure (pseudo-spectral procedure) is more efficient than a direct convolution product since the FFT computation time scales as $n \log n$. However, the finite resolution used in this procedure generates a numerical artefact commonly known as the 'aliasing' effect (apparition of non-physical waves near the Nyquist frequency). This effect may be handled through a de-aliasing procedure, in which the non-linear terms are computed with a resolution 3/2 higher than the effective resolution used in the source terms (e.g. Peyret 2002).

Comparing our spectral code with a ZEUS-type finite difference code (Stone & Norman 1992), similar results are obtained with a finite difference resolution two to three times higher than the spectral resolution. However, FFT calculations are more computationally expensive than finite differences, leading to a final computational time equivalent for both kinds of code with the same 'effective' resolution.

All the simulations presented in this paper were performed with an *xyz* resolution of $128 \times 64 \times 64$ with an aspect ratio of $4 \times 1 \times 1$, *x* being the azimuthal direction, *y* the radial direction and *z* the vertical direction. One may change the physical viscosity and resistivity as well as the magnetic field intensity (β). The mean magnetic field (conserved in the simulations due to the adopted boundary conditions) is aligned in the *z*-direction. White noise initial perturbations with respect to the laminar flow are introduced as initial conditions on all variables. With $\beta = 100$, $Pm = 1$ and $Re = 3200$ one typically generates flow snapshots as shown in Fig. 5 after
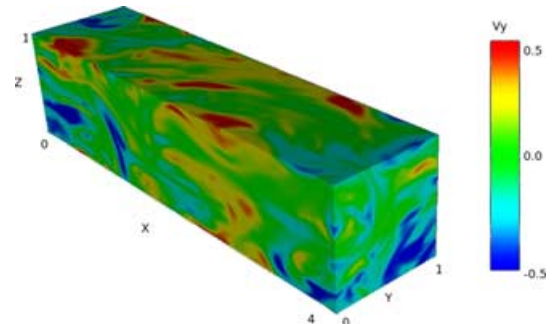

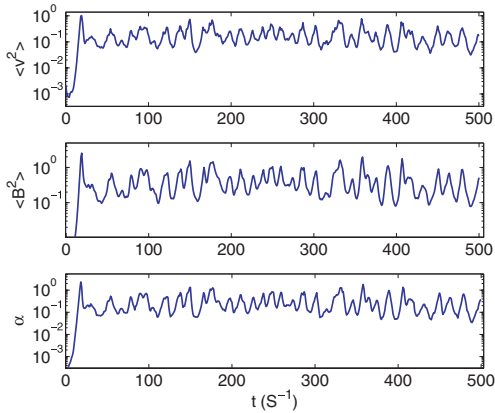**Figure 5.** w_y plot (radial velocity) for $\beta = 100$, $Re = 3200$.

Figure 6. $\beta = 100$, $Re = 3200$ run.

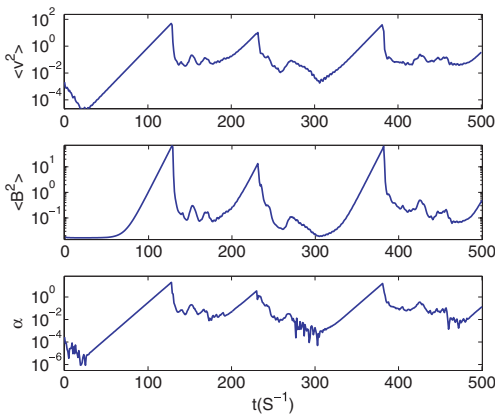**Figure 7.** $\beta = 30$, $Re = 3200$ run.

relaxation of transients; this flow is quite characteristic of a fully developed 3D turbulent field.[3]

3.4 MRI behaviour near the instability threshold

The MRI is a weak magnetic field instability, which should be quenched for $\beta \lesssim 1$ in astrophysical discs. Since the MRI is assumed to be the source of momentum transport in discs, and as at least some discs are expected to be close to equipartition if they are to support magnetically driven ejection (Ferreira 1997), one may wonder if this instability is efficient enough in the vicinity of the strong magnetic field stability threshold. We investigate this question in an unstratified context here (the absence of stratification significantly raises the β stability threshold).

We present two simulations. In the first one, $\beta = 100$ and $Re = 3200$ (run 1); this run reproduces typical results from the literature. The second simulation is performed close the β threshold, that is, for $\beta = 30$ and $Re = 3200$. The time development of some important quantities is depicted in Figs 6 and 7 for these two runs. One immediately notices a marked difference between these two simulations. On run 1, we find a classical MRI behaviour, as studied by Hawley et al. (1995), characterized by $\alpha \sim 10^{-1}$ and random fluctuations of all statistical quantities. However, run 2 exhibits strong

[3] Movies of some of the simulations presented in this paper may be found on the web at http://www-laog.obs.ujf-grenoble.fr/public/glesur/index.htm.

exponential growth ('bursts') for about 100 shear times ($\sim$10 orbits), and a sudden drop of fluctuation amplitudes. This behaviour is explained as follows: for such low β only the largest wavelength mode is unstable (and not smaller scales); the mode amplitude increases for many shear times, as this mode is an exact non-linear solution to the incompressible equations of motions (Goodman & Xu 1994). We therefore observe the growth of the channel flow as seen by Hawley & Balbus (1992). However, as this channel solution reaches sufficiently large amplitude, secondary instabilities such as the Kelvin–Helmoltz instability quickly set in and destroy these ordered motions, and a new cycle starts (see Goodman & Xu 1994 for a detailed description of these secondary instabilities).

Note that this kind of behaviour and related explanation does also apply to the low Reynolds threshold, since there the smallest scales are viscously damped and only the largest ones remain unstable. We did observe this behaviour close to the low Reynolds threshold, as did Fleming et al. (2000) but in an indirect way (see figs 2 and 4 of their paper), and one can conclude that these bursts are characteristic of a marginally unstable MRI. Such bursts may be astrophysically relevant. Indeed, one may wonder about the MRI behaviour close to the dead zone (Gammie 1996), where presumably the magnetic Reynolds number is small, and the instability quenched. If these bursts exist in real discs, they may quickly destroy this dead zone under the effects of the strong turbulent motions observed in our simulations.

Let us have a closer look on these bursts with the help of correlation lengths defined as

$$L_i = \frac{\int \mathrm{d}y_i \int f(x_i) f(x_i - y_i) \mathrm{d}x_i}{\int f^2(x_i) \mathrm{d}x_i}, \tag{26}$$

where $i = 1, 2, 3$ are the directions of correlation and f refers either to the velocity or to the magnetic field. Note that with this definition, the correlation length vanishes in the z-direction for a pure sinusoidal signal, and equals 1 in the y-direction for a channel flow, as a consequence of the shearing sheet boundary conditions. Therefore, these correlation lengths provide us with a convenient tool to trace the presence of the channel flow solution in our simulations. We show in Figs 8 and 9 the evolution of the correlation length in the y- and z-directions for the w_x field (a similar behaviour is obtained with the other field components). The behaviour of correlation lengths closely follows what can be seen by monitoring the energy in the deviations from the laminar flow (Fig. 7), and indicates the presence of two main regimes in this simulation. The first regime corresponds to an exponential growth ('burst') of the channel flow, for which L_y is found to be equal to the box size and
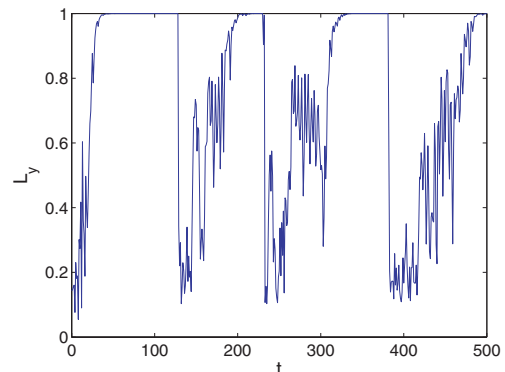

Figure 8. Correlation length of w_x in the y-direction as a function of time, $\beta = 30$.
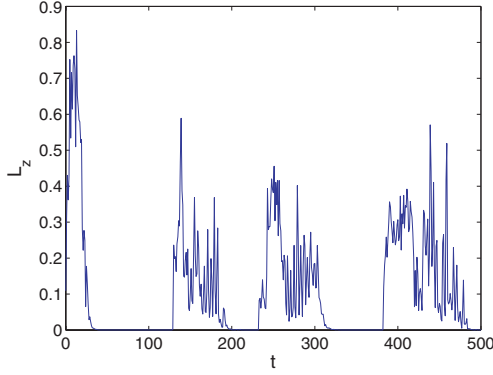
Figure 9. Correlation length of w_x in the z-direction as a function of time, $\beta = 30$.

Figure 10. Prandtl effect for $\beta = 100$.

$L_z = 0$ (a careful examination shows that L_z is exponentially decaying down to 10^{-10}), indicating the presence of a purely sinusoidal mode in the z-direction in the burst stage. The second regime is a more classical state for 3D turbulent motion, with $L_y \simeq 0.5$ and $L_z \simeq 0.4$. Note that L_y grows on very short time-scales, leading eventually to a new burst stage.

These correlation lengths disclose numerical artefacts in the first regime. In a real disc, one would expect a loss of correlation in the radial direction on a scale of the order of a few scaleheights: indeed, the typical frequency involved in these phenomena is of the order of the Keplerian frequency and a signal cannot propagate faster than the sound speed, leading to a maximum correlation length of a few scaleheights.

Similarly, the vanishingly small vertical correlation length for the channel flow solution is also an artefact of the adopted boundary conditions. A more realistic result would follow if one were to take into account the vertical stratification and set the boundary conditions far enough from the disc mid-plane. More generally, our results are probably not directly applicable to a real disc, but they shed some light on what the generic behaviour of the MRI would look like near various stability thresholds, even though different aspect ratio and boundary conditions should be investigated before firm conclusions can be drawn.

Finally, the behaviour exemplified in our simulations suggests that assuming α constant would poorly represent the transport behaviour close enough to the marginal stability limit. Time-dependent transport models are needed in such a context. Real discs may not operate close to the strong-field limit unless some (unknown) back-reaction loop is at work, or unless (more realistically) the magnetic field varies in a systematic way with radius throughout the disc; consequently, the bursting behaviour observed here may imply a similar ejection variability in the relevant regions of jet-driving discs. Note however that our 'mean' equivalent α is rather large ($\alpha \simeq 5$), leading us to question the role of the ignored fluid compressibility in these cases; it is quite possible that couplings to compressible modes may effectively limit the magnitude of the bursts.

3.5 Magnetic Prandtl dependence of transport coefficients

All previously published simulations were performed without numerical control of the dissipation scales and dissipation processes. However, as pointed out earlier, such a control is required to ascertain convergence. In this section, the role of the Reynolds and Prandtl numbers defined in Section 3 is examined. In particular, the
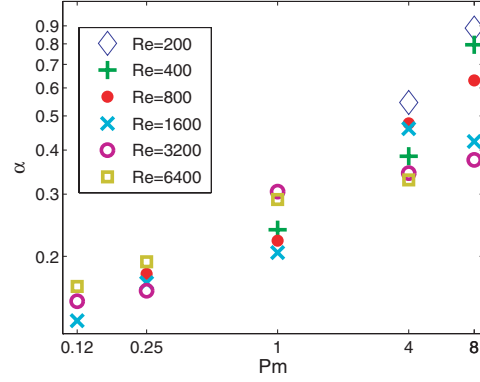
Prandtl number allows us to change the ratio of the viscous and resistive dissipation scales. Unfortunately, deviations from $Pm = 1$ are quite demanding numerically, since one wants to resolve both the velocity and magnetic dissipation scales. We present in Fig. 10 the result of such simulations: we plot the mean transport coefficient (α) as a function of the Prandtl number, for various Reynolds numbers (the Reynolds number quantifies the viscous dissipation scale). Statistical averages are computed over 500 shear times, and start after the first 100 shear times to avoid pollution by relaxation of the initial transient dynamics. From these plots, one finds a significant correlation between the Prandtl number and the transport coefficient, leading to

$$\alpha \propto Pm^\delta \qquad \text{for} \begin{cases} 0.12 < Pm < 8 \\ 200 < Re < 6400 \end{cases}, \qquad (27)$$

with δ in the range 0.25–0.5. Note that this result shows that the transport coefficient depends on Re and Rm via Pm, at least in the Pm range considered in this paper. This may be seen in Fig. 10 as a small vertical dispersion (variation of both Re and Rm at constant Pm) compared to the effect of a single Pm change. Although this section is the briefest of the paper, this result constitutes the most important finding of this investigation (and the most computationally intensive one!).

Note that the numerical results obtained at very high Reynolds number and high Prandtl number are only marginally resolved, mainly because of a very short magnetic dissipation scale. This remark may explain that the two points at $Pm = 8$ lie somewhat below the mean of the other results. Our preliminary tests at higher resolution seem to show that a higher transport obtains at higher resolution at $Pm = 8$ and $Re = 6400$, which confirms a limit due to resolution in these high Pm runs. This behaviour is easily understood, since the finite numerical resolution enforces a numerical dissipation scale (roughly equal to the grid scale), which is obviously the same for the magnetic and velocity fields. Therefore, at high Pm, the effective magnetic dissipation scale is forced to be larger than the expected one, leading to an altered spectral distribution and a smaller 'numerical Prandtl'.

One may wonder if this Prandtl dependence may be correlated to the linear growth rates discussed before. To this effect, we plot the linear growth rate of the largest mode for the different simulations used for this study in Fig. 11. Similar results follow when replacing the growth rate of the largest mode by the maximum growth rate. Although the idea of a transport efficiency controlled by the linear growth rate is widely spread in the astrophysical community, this plot shows us that, at least for this example, the linear growth rate
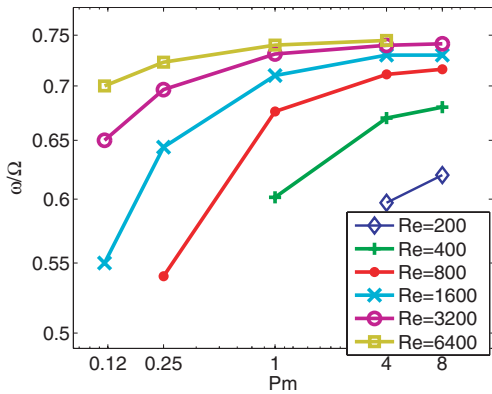
Figure 11. Linear growth rate of the largest mode for various (*Re*, *Pm*) at $\beta = 100$.

does not explain the transport behaviour observed in Fig. 10. Moreover, it appears that, as one may suspect from equation (13), the growth rate is not controlled only by *Pm*, but also by some complex combination of *Re* and *Rm*. Umurhan, Menou & Regev (2007) tried to get this kind of α–*Pm* correlation analytically, using a weakly non-linear analysis of the channel flow. This study leads to a stronger α–*Pm* correlation with $\delta = 1$ in the limit $Pm \ll 1$, which appears to be quite different from our full 3D numerical results. Note however that their analysis belongs to very different boundary conditions (rigid instead of shearing sheet) and the results are therefore not of direct relevance to our numerical investigation; nevertheless both studies point out the role of the Prandtl number. In any case, one needs to find some full non-linear theory to explain the transport dependence on *Pm*.

The observed correlation indicates the existence of a back reaction of the small magnetic field scales on the large ones (at least for the range of Reynolds and Prandtl numbers explored here). Note that this effect is expected to saturate at some point, since in the limit $Pm \to 0$ with $Re \to \infty$ and Rm kept constant, equation (27) predicts a vanishing transport in spite of the existence of the linear instability. This issue is further discussed in Section 4, the Reynolds number limitation of our investigation being the most serious here. In any case, the exact implications of these findings remain to be understood, but may potentially be quite important since the Prandtl number varies by many orders of magnitude in astrophysical objects. For example, Brandenburg & Subramanian (2005) suggest that values as small as $Pm \sim 10^{-8}$ might be found in YSOs, while $Pm \sim 10^4$ would be more typical of AGN discs. These estimates are highly uncertain; even a substantially narrower range is of course out of reach of present-day computers.

Finally, this kind of back reaction points out the potential role of small-scale physics (dissipation scales) on the properties of turbulence at the largest available scales (disc height scale). This argues for a careful treatment of the role of dissipation and reconnection processes on the turbulence transport characterization.

4 DISCUSSION

In this paper, we have investigated the role of local dimensionless numbers on the efficiency of the dimensionless turbulent transport. To this effect, we have first generalized previously published linear stability limits, to account for the presence of both viscous and resistive dissipation. Namely, we have confirmed in all cases that the large-field marginal stability limit is characterized by a constant

plasma β parameter, of the order of 30 in the shearing sheet unstratified context (but more likely of the order of unity in real, stratified discs). When marginal stability follows from dissipation and not magnetic tension stabilization, we have found that the marginal stability limit is captured by two asymptotic regimes: a large Reynolds (*Re*), small magnetic Reynolds (*Rm*) one, with a marginal stability limit $Rm \sim \beta^{1/2}$, and a small Reynolds, large magnetic Reynolds number one, where $ReRm \sim 10^2 \beta^{1/2}$. A phenomenological explanation has been provided for this behaviour.

In the previous section, we have investigated the behaviour of the MRI near the low-β instability threshold; in our simulations, $\beta = 30$, a value representative of the large-field threshold in our simulation box. In vertically stratified discs, this threshold obtains for much smaller values, typically $\beta \sim 1$ (Gammie & Balbus 1994). We found, somewhat unexpectedly, that turbulent transport is significantly enhanced through burst events, even surprisingly close to the marginal stability threshold. As pointed out earlier, this behaviour is physical and not numerical. The use of periodic boundary conditions (vertical) or semiperiodic (radial) boundary conditions may enhance the role of the channel flow solution which is responsible for this behaviour, and a real disc channel flow may break up sooner than observed in our local simulations, leading to smaller burst magnitudes. Moreover, $\alpha > 1$ leads to supersonic motions and compressible numerical simulations are needed to properly quantify the phenomenon, which may exhibit new secondary compressible instabilities in such a context. All these issues lead to the conclusion that low-β MRI would produce weaker bursts and therefore smaller transport coefficients than observed in our simulation. However, there is no physical reason why the turbulence bursts would be suppressed, and we believe that these bursts may be a strong signature of regions of stratified discs where MRI-driven turbulence is driven close to the marginal stability threshold.

The most important new result reported in this paper is a correlation between the transport efficiency, and the magnetic Prandtl number, leading to a higher transport coefficient for larger Prandtl numbers. As in the case of the bursting behaviour discussed above, the boundary conditions used in these simulations play some role in the result. However, the possible biases are less obvious and tests with plane radial walls need to be performed to get a grasp on boundary condition effects. Moreover, one needs to check the correlation at higher resolutions, and if possible higher Prandtl numbers, using different kinds of codes to get a better characterization and a physical description of the phenomena involved in this observation.

More specifically, a puzzling fact points towards a potential bias due to the shearing sheet boundary conditions. In non-magnetized shear flows, transport in the subcritical regime, far enough from the marginal stability limit scales like $1/Rg$ where Rg is the subcritical transition Reynolds number (Lesur & Longaretti 2005). Closer to the marginal stability limit, and in the supercritical regime (e.g. when the Rayleigh stability criterion is not satisfied), transport is enhanced with respect to this scaling, but one always has $\alpha < 1/Rc$ where Rc is the critical Reynolds number of linear instability. However, for MRI-driven turbulence, one has $\alpha >$ or $\gg 1/Rc$, as can be checked from our results. Close to the marginal stability limit, this enhanced efficiency is related to the existence of the channel flow solution, as discussed above. As each linear mode is a non-linear solution to the incompressible problem, one may ask whether this enhanced transport, which is observed also far from the marginal stability limit, is not an artefact of the shearing sheet boundary condition, which allows such non-linear coherent modes to develop. This behaviour is not necessarily unphysical or irrelevant to actual disc systems, but this point needs to be checked in the future.

Finally, let us come back to the magnetic Prandtl number dependence of α. As pointed out earlier, the dependence of the transport efficiency on the magnetic Prandtl number indicates a back reaction of small scales on large ones. We make here a few comments on this feature. In particular, we shall argue that this behaviour must saturate at low and large enough *Pm*. The magnetic Prandtl number is related to the ratio of the viscous l_ν and resistive l_η dissipation scales, the exact relation depending on the shape of the turbulent energy spectrum. Generally speaking, the Prandtl number varies monotonically with the ratio l_ν/l_η, and one expects $Pm \ll 1$ (respectively $Pm \gg 1$) when $l_\nu/l_\eta \ll 1$ (respectively $l_\nu/l_\eta \gg 1$). The spectrum of the largest scales tends to be flatter than usual turbulent spectra due to the role of the linear instability, down to the scale where the magnetic tension prevents the instability from occurring (most probably, this 'instability sector' of the spectrum only represents a small part of the overall turbulent spectra of actual discs, because of their enormous Reynolds numbers). Leaving aside these largest scales, for $Pm \ll 1$, the spectrum is expected to be Kolmogorovian and anisotropic down to the resistive dissipation scale (Goldreich & Sridhar 1995), while below this scale and down to the viscous scale, the velocity spectrum is the usual Kolmogorov velocity spectrum and the magnetic spectrum drops much faster. On the other hand, for $Pm \gg 1$, the spectrum should be Kolmogorovian down to the viscous dissipation scale (Goldreich & Sridhar 1995), while the magnetic spectrum should scale like k^{-1} below the viscous dissipation scale and down to the resistive scale (Cho, Lazarian & Vishniac 2003). It is therefore tempting to see in a difference of accumulation of magnetic energy at small scales the cause of the back reaction of these scales to the largest ones, which would create the observed magnetic Prandtl number dependence of the turbulent transport efficiency. Nevertheless, in both small and large Prandtl number settings, turbulent motions in the inertial range are random in phase, so that one expects that to lowest order, coupling of the turbulent spectrum with the largest MRI unstable scales vanishes. To next order, the steepness of the Kolmogorov spectrum indicates that the strength of the coupling decreases with increasing Reynolds number in the vicinity of the viscous dissipation scale, suggesting that at large enough Reynolds numbers, the Prandtl dependence should saturate (a potential caveat to this argument being the possible role played by a small-scale field generation through dynamo action). Such a saturation was not observed in our simulations, although a weak dependence of our results on the magnitude of the Reynolds number may be detected in Fig. 10; however, such an effect might also arise from resolution requirements, which makes our lower Reynolds number results confined to the larger Prandtl number range. Unfortunately, our results can hardly be improved upon with the present generation of computers, leaving the question of the Reynolds number saturation of the Prandtl number dependence open, as well as the overall difference in transport efficiency between the small and large Prandtl number cases. Resolving this issue is crucial to ascertain the role of the MRI in disc transport.

REFERENCES

Arlt R., Urpin V., 2004, A&A, 426, 755
Balbus S. A., 2003, ARA&A, 41, 555
Balbus S. A., Hawley J. F., 1991, ApJ, 376, 214
Balbus S. A., Hawley J. F., 2003, in Falgarone E., Passot T., eds, LNP Vol. 614, Turbulence and Magnetic Fields in Astrophysics. Springer, Berlin, p. 329
Balbus S. A., Terquem C., 2001, ApJ, 552, 235
Balbus S. A., Hawley J. F., Stone J. M., 1996, ApJ, 467, 76
Blaes O. M., Balbus S. A., 1994, ApJ, 421, 163
Brandenburg A., Subramanian K., 2005, Phys. Rep., 417, 1
Brandenburg A., Nordlund A., Stein R. F., Torkelsson U., 1995, ApJ, 446, 741
Cho J., Lazarian A., Vishniac E. T., 2003, ApJ, 595, 812
Dubrulle B., Marié L., Normand C., Richard D., Hersant F., Zahn J.-P., 2005, A&A, 429, 1
Ferreira J., 1997, A&A, 319, 340
Fleming T. P., Stone J. M., Hawley J. F., 2000, ApJ, 530, 464
Gammie C. F., 1996, ApJ, 457, 355
Gammie C. F., Balbus S. A., 1994, MNRAS, 270, 138
Gardiner T. A., Stone J. M., 2005, in de Gouveia dal Pino E. M., Lugones G., Lazarian A., eds, AIP Conf. Proc. Vol. 784, Magnetic Fields in the Universe: From Laboratory and Stars to Primordial Structures. Am. Inst. Phys., New York, p. 475
Goldreich P., Sridhar S., 1995, ApJ, 438, 763
Goodman J., Xu G., 1994, ApJ, 432, 213
Hawley J. F., 2000, ApJ, 528, 462
Hawley J. F., Balbus S. A., 1992, ApJ, 400, 595
Hawley J. F., Gammie C. F., Balbus S. A., 1995, ApJ, 440, 742
Hawley J. F., Balbus S. A., Winters W. F., 1999, ApJ, 518, 394
Ji H., Goodman J., Kageyama A., 2001, MNRAS, 325, L1
Ji H., Burin M., Schartman E., Goodman J., 2006, Nat, 444, 343
Johnson B. M., Gammie C. F., 2006, ApJ, 636, 63
Klahr H. H., Bodenheimer P., 2003, ApJ, 582, 869
Lesur G., Longaretti P.-Y., 2005, A&A, 444, 25
Peyret R., 2002, Spectral Methods for Incompressible Viscous Flow. Springer, New York
Richard D., 2001, PhD thesis, Université de Paris VII
Richard D., Zahn J., 1999, A&A, 347, 734
Rüdiger G., Shalybkov D., 2002, Phys. Rev. E, 66, 016307
Shakura N. I., Sunyaev R. A., 1973, A&A, 24, 337
Shalybkov D., Ruediger G., 2005, A&A, 438, 411
Stone J. M., Norman M. L., 1992, ApJS, 80, 753
Stone J. M., Hawley J. F., Gammie C. F., Balbus S. A., 1996, ApJ, 463, 656
Turner N. J., Sano T., Dziourkevitch N., 2007, ApJ, 659, 729
Umurhan O. M., Menou K., Regev O., 2007, Phys. Rev. Lett., 98, 034501
Urpin V., 2003, A&A, 404, 397
Wardle M., 1999, MNRAS, 307, 849

This paper has been typeset from a TEX/LATEX file prepared by the author.